Meas. Sci. Technol. **20** (2009) 074005 (14pp) doi:10.1088/0957-0233/20/7/074005

Surface pressure and aerodynamic loads determination of a transonic airfoil based on particle image velocimetry

D Ragni, A Ashok, B W van Oudheusden and F Scarano

Faculty of Aerospace Engineering, Delft University of Technology, Delft, The Netherlands

E-mail: D.Ragni@tudelft.nl

Received 28 July 2008, in final form 12 December 2008
Published 21 May 2009
Online at stacks.iop.org/MST/20/074005

Abstract
The present investigation assesses a procedure to extract the aerodynamic loads and pressure distribution on an airfoil in the transonic flow regime from particle image velocimetry (PIV) measurements. The wind tunnel model is a two-dimensional NACA-0012 airfoil, and the PIV velocity data are used to evaluate pressure fields, whereas lift and drag coefficients are inferred from the evaluation of momentum contour and wake integrals. The PIV-based results are compared to those derived from conventional loads determination procedures involving surface pressure transducers and a wake rake. The method applied in this investigation is an extension to the compressible flow regime of that considered by van Oudheusden *et al* (2006 Non-intrusive load characterization of an airfoil using PIV *Exp. Fluids* **40** 988–92) at low speed conditions. The application of a high-speed imaging system allows the acquisition in relatively short time of a sufficient ensemble size to compute converged velocity statistics, further translated in turbulent fluctuations included in the pressure and loads calculation, notwithstanding their verified negligible influence in the computation. Measurements are performed at varying spatial resolution to optimize the loads determination in the wake region and around the airfoil, further allowing us to assess the influence of spatial resolution in the proposed procedure. Specific interest is given to the comparisons between the PIV-based method and the conventional procedures for determining the pressure coefficient on the surface, the drag and lift coefficients at different angles of attack. Results are presented for the experiments at a free-stream Mach number $M = 0.6$, with the angle of attack ranging from 0° to 8°.

Keywords: PIV, aerodynamic loads measurement, transonic airfoil

1. Introduction

Experimental determination of aerodynamic loads is conventionally performed by means of force balances and/or surface pressure taps and Pitot-tube wake rakes. While these measurement techniques have proven to be reliable and accurate, they require instrumentation and modifications of the model, provide information only at discrete points (the pressure tap locations) and in some cases have an intrusive effect in the flow (e.g. wake rakes). Moreover, the relation between the loads on the body and the flow-field structure requires additional interpretation, which becomes even more relevant when dealing with unsteady flow phenomena. In the recent past years, nonintrusive measurement techniques have enabled the determination of loads-related fluid dynamic quantities at relatively high spatial resolutions. In particular, pressure sensitive paint (PSP) has demonstrated its capabilities in determining surface pressure and aerodynamic force coefficients, provided that the flow is exerting a considerable pressure on the surface model (McLachlan and Bell 1995). The sensitivity of the technique to temperature, however, may limit its application in flows where thermal effects are not negligible (Klein *et al* 2005).

Concerning nonintrusive techniques, particle image velocimetry (PIV) has demonstrated its potential for the purpose of determining the aerodynamic forces on airfoils,

 © 2009 IOP Publishing Ltd Printed in the UK

comparing favorably with the values obtained by wake-rake and force balances (see e.g. Sjörs and Samuelsson (2005), De Gregorio (2006), van Oudheusden *et al* (2006)). In order to compute aerodynamic coefficients from flow field data, the momentum equation is used in its integral form, while the pressure can be derived from the velocity data through the integration of its differential expression. In the case of incompressible flow, the pressure field can be related directly to velocity through Bernoulli's equation provided that the flow is irrotational. For rotational flows, the pressure gradient is computed from the momentum equation in differential form, and the pressure field obtained by subsequent spatial integration, for example by means of a space-marching technique (see e.g. Baur and Köngeter (1999)). For compressible flows, the procedure is analogous and the same approach can be followed, provided that the method accounts for the variable density.

The objective of the present study is to evaluate the feasibility of obtaining accurate information on the pressure distribution and the aerodynamic coefficients from PIV-based measurements for an airfoil under transonic flow conditions. Additional pressure-based measurements of integral forces and surface pressure distributions were simultaneously performed as a means of validating the PIV procedure, as done previously for a low-speed airfoil under incompressible flow conditions (van Oudheusden *et al* 2006). Some aspects of the implementation of a PIV-based loads determination technique in the supersonic flow regime at Mach 2 have been addressed by Souverein *et al* (2007), introducing the treatment of shock waves in the field as an additional problem.

2. Theoretical background

2.1. Integral force determination

The force acting on a body immersed in a fluid is the result of the surface pressure and shear stress distributions. Application of the integral momentum conservation concept permits the integral forces acting on the body to be computed from their reaction on the flow, without the need to evaluate the flow quantities at the surface of the model (Anderson 1991). A schematic of the approach is depicted in figure 1, where the rotational viscous flow domain in the wake of the airfoil is schematically represented by the shaded region.

Assuming a two-dimensional flow field that is steady in the statistical sense, Reynolds averaging can be applied to yield the momentum equation in its integral form, which relates the resultant aerodynamic force $\vec{R}$ on the airfoil to a contour integral around it:

$$\vec{R} = -\oint\!\!\oint_S \rho(\vec{V}\cdot\vec{n})\,\vec{V}\,\mathrm{d}s + \oint\!\!\oint_S (-p\vec{n} + \bar{\bar{\tau}}\cdot\vec{n})\,\mathrm{d}s. \qquad (1)$$

In the above formulation, S is an arbitrary integration contour surrounding the airfoil, composed of infinitesimal elements ds, with $\vec{n}$ being the outward pointing normal vector. The terms on the right-hand side represent the mean flow momentum,

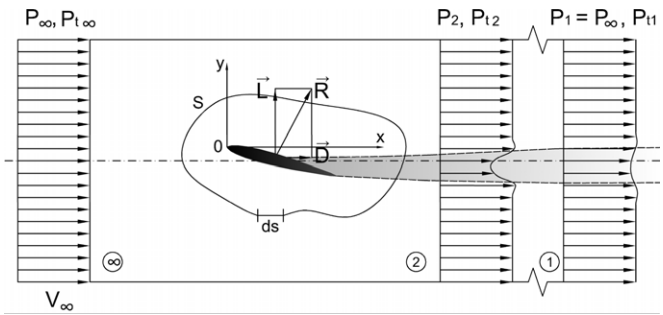

Figure 1. Schematic of the control volume approach for the loads determination.

the pressure and stress contribution, the latter incorporating both viscous and turbulence effects. Viscous stresses along the contour are neglected, as they do not play a significant role in this case, but turbulent stresses will be maintained in the discussion because of their influence for some cases. Note that all variables are to be interpreted in their (Reynolds-) averaged sense; for simplicity of notation, an overbar denoting averaging will only be applied explicitly where turbulence terms are concerned.

To reduce the impact of uncertainty in the momentum flux along the contour on the integral value, the free-stream momentum is subtracted from the local momentum flux value, which transforms equation (1) into the equivalent but more robust expression:

$$\vec{R} = -\oint\!\!\oint_S \rho(\vec{V}\cdot\vec{n})\,(\vec{V}-\vec{V}_\infty)\,\mathrm{d}s + \oint\!\!\oint_S (-p\vec{n} + \bar{\bar{\tau}}\cdot\vec{n})\,\mathrm{d}s. \qquad (2)$$

The resultant aerodynamic force may be resolved into the components of lift and drag with respect to a Cartesian frame of reference aligned with the free-stream direction, where the origin is placed at the leading edge of the airfoil. Correspondingly, the contour integral may be expanded in Cartesian components to provide the differential contributions of the contour integral to drag and lift, respectively:

$$\begin{cases} \mathrm{d}D = \underbrace{\rho u(u-U_\infty)\,\mathrm{d}y - \rho v(u-U_\infty)\,\mathrm{d}x}_{\text{Mean momentum}} \\ \qquad + \underbrace{\rho(\overline{u'u'})\,\mathrm{d}y - \rho(\overline{u'v'})\,\mathrm{d}x}_{\text{Turbulent stresses}} + \underbrace{p\,\mathrm{d}y}_{\text{Pressure}} \\ \mathrm{d}L = \underbrace{\rho(uv)\,\mathrm{d}y - \rho(vv)\,\mathrm{d}x}_{\text{Mean momentum}} \\ \qquad + \underbrace{\rho(\overline{u'v'})\,\mathrm{d}y - \rho(\overline{v'v'})\,\mathrm{d}x}_{\text{Turbulent stresses}} - \underbrace{p\,\mathrm{d}x}_{\text{Pressure}}. \end{cases} \qquad (3)$$

All the flow quantities are assumed to be known along the contour. Two-component PIV can provide the kinematical quantities in the first two groups of contributions in equation (3), mean momentum and turbulent stresses, but the

pressure as well as the variable density have to be inferred from the velocity fields by additional steps (see section 2.2). Computation of drag and lift then involves evaluating equation (3) around the entire contour. The accumulation of errors or uncertainties in the measurement data along the contour will propagate into the uncertainty on the resulting integral forces values. In particular, for the drag coefficient this can lead to inaccurate computed values (van Oudheusden *et al* 2006). This can be alleviated by using a wake-traverse approach, for which in the present investigation the method proposed by Jones (1936) is used, with adaptations for compressibility effects. The particular method is explained in figure 1, where index 1 denotes an imaginary x-station far behind the model where the static pressure has recovered to p_∞. Direct application of the control volume method for the drag computation could then be limited to consider only the momentum deficit at station 1. However, during experiments the wake measurements are typically performed in a measurement plane at station 2, which is closer to the model and in an environment where the pressure has not recovered to p_∞ due to the presence of the model. The concept of mass conservation is invoked to relate the drag to the measured properties in the measurement plane 2:

$$D = \int \rho_1 u_1 (U_\infty - u_1)\,\mathrm{d}y_1 = \int \rho_2 u_2 (U_\infty - u_1)\,\mathrm{d}y_2. \tag{4}$$

Next, the value of u_1 is computed by assuming that between stations 1 and 2 the total pressure remains constant along streamlines and that the effect of turbulent stresses is negligible, allowing it to be related to the total pressure at the actual measurement station 2. In the case of incompressible flow this results in Jones' original expression for the drag coefficient:

$$c_d = 2 \int \sqrt{\frac{p_{t2} - p_2}{q_\infty}} \left(1 - \sqrt{\frac{p_{t2} - p_\infty}{q_\infty}}\right) \mathrm{d}\left(\frac{y_2}{c}\right) \tag{5}$$

while accounting for flow compressibility the drag coefficient may be computed as

$$c_d = 2 \int \left(\frac{p_2}{p_\infty}\right)^{\frac{1}{\gamma}} \cdot \left(\frac{p_{t_2}}{p_{t_\infty}}\right)^{\frac{\gamma-1}{\gamma}} \cdot \sqrt{\frac{1-(p_2/p_{t_2})^{\frac{\gamma-1}{\gamma}}}{1-(p_\infty/p_{t_\infty})^{\frac{\gamma-1}{\gamma}}}\left[1 - \frac{1-(p_\infty/p_{t_2})^{\frac{\gamma-1}{\gamma}}}{1-(p_\infty/p_{t_\infty})^{\frac{\gamma-1}{\gamma}}}\right]}\,\mathrm{d}\left(\frac{y_2}{c}\right). \tag{6}$$

As shown in equation (6), the static and total pressure in the PIV wake measurements and the values in the free stream are required for the drag evaluation. Moreover, in order to optimize the procedure, the integration can be limited to include only the flow region where the total pressure is different from its free-stream value. As a consequence, the drag coefficient can be computed at an increased spatial resolution that allows resolving the momentum deficit in the wake, provided that the whole wake is captured in the field of view. The computation of the lift coefficient, however, requires the measurement of the flow field along a contour surrounding the body, which can be achieved only by a relatively larger field of view. As a consequence, the wake becomes not properly resolved because of the lowered resolution; however, this does not have a significant effect on the lift values, the momentum deficit in the wake not being as relevant for the lift as it is for the drag.

2.2. Pressure determination

In the region of the flow that can be assumed to behave as adiabatic and inviscid, the isentropic relations (Anderson 2003) can be used to compute the pressure from the local velocity:

$$\frac{p}{p_\infty} = \left(1 + \frac{\gamma - 1}{2} M_\infty^2 \left(1 - \frac{V^2}{V_\infty^2}\right)\right)^{\frac{\gamma}{\gamma-1}}, \tag{7}$$

with $V = |\vec{V}|$ being the velocity magnitude. In rotational and viscous flow regions, for the major part represented by the wake, a different strategy needs to be applied for the pressure determination in the flow field. Here, the pressure gradient is computed from the momentum equation in differential form and subsequently the pressure is integrated from the gradient field. For viscous flows the Navier–Stokes equations apply, but in regions where the viscous terms have a negligible effect, the Euler equations can be used instead. Assuming further adiabatic flow and perfect gas behavior, an explicit approach for the pressure gradient evaluation can then be derived from the momentum equation (van Oudheusden *et al* 2007), to yield

$$-\frac{\vec{\nabla} p}{p} = -\vec{\nabla} \ln(p/p_\infty) = \frac{\gamma M_\infty^2}{V_\infty^2 + \frac{\gamma-1}{2} M_\infty^2 (V_\infty^2 - V^2)} \cdot (\vec{V} \cdot \vec{\nabla})\vec{V}. \tag{8}$$

This formulation simplifies the pressure integration, since it incorporates the effect of variable density, while still permitting a non-iterative solution approach. More extensive details of the pressure gradient evaluation in compressible flows, including how the effect of the turbulent stresses may be included, can be found in van Oudheusden (2008). The spatial integration of the pressure gradient in order to compute the pressure fields is in this study performed with a space-marching algorithm (van Oudheusden 2008), imposing isentropic pressure as the boundary condition in the free stream.

3. Experimental apparatus and procedure

3.1. Wind tunnel and airfoil model

The experimental investigation was performed in the transonic–supersonic wind tunnel (TST-27) of the Aerodynamics Laboratories at the Delft University of Technology. The facility is a blow-down-type wind tunnel that can achieve Mach numbers in the range from about 0.5 to 4.2 in a test section of dimension of about 0.280 m (width) × 0.250 m (height). The wind tunnel is fed from a 300 m^3 storage vessel with a maximum pressure of 42 bar, while the tunnel

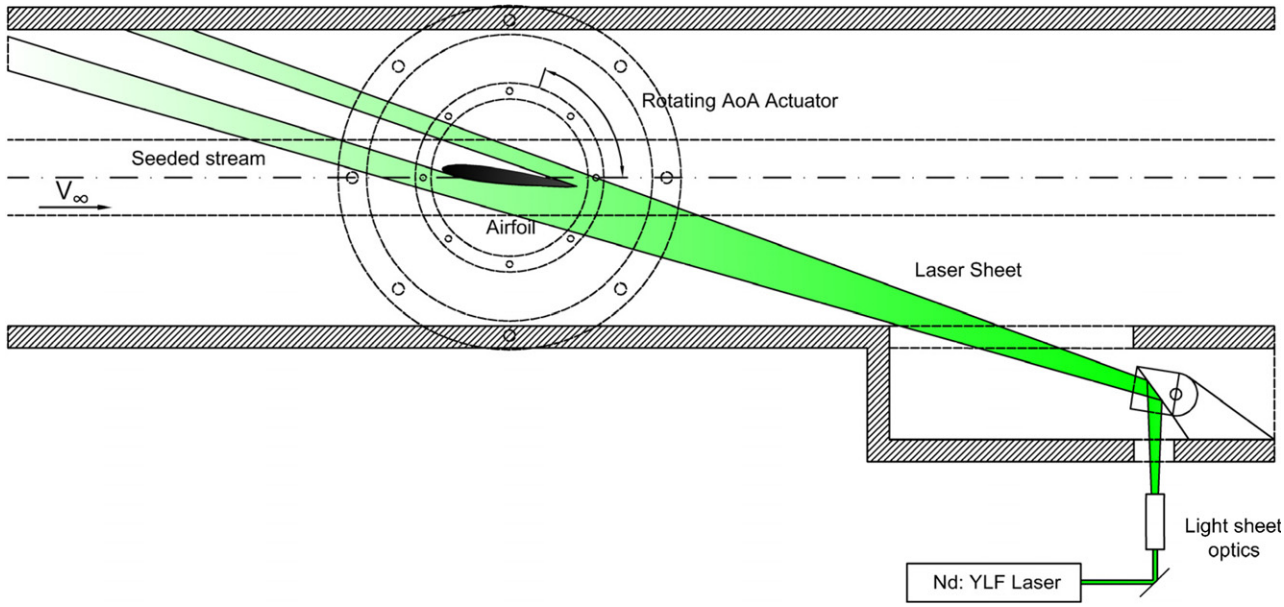

Figure 2. Schematic of the PIV arrangement, seeding and illumination.

regulating system maintains a stagnation pressure of 1.935 ± 0.001 bar. The choke section was set to obtain free-stream Mach numbers in the range from 0.60 ± 0.01 to 0.80 ± 0.01. The flow conditions for the results reported in the present communication are $M = 0.60 \pm 0.01$ and Reynolds chord number 2.2×10^6.

The experimental set-up is schematically depicted in figure 2, which shows the model positioned in the wind tunnel test section, as well as the PIV illumination arrangement. The model is a NACA 0012-30 airfoil, with a nominal chord of 100 mm. The model is installed between the glass windows in the sidewalls, which permits the rotation by a manual actuator to set the angle of attack. The latter has been varied in the range 0°–8°, set by means of a digital tilt-scale, the inaccuracy of which is estimated at 0.1°.

The airfoil model is equipped with 20 pressure orifices to obtain pressure data on the surface of the airfoil, which can be compared with PIV-based surface pressure determination, as well as to determine the lift coefficient through the integration of the surface pressure distribution. As shown in figure 3, the orifice locations are such that they provide pressure data over only one side of the model. Employing the symmetry of the airfoil, the complete pressure distribution of the model is obtained by performing two separate experiments with the airfoil under positive and negative incidence, respectively. In order to check for the consistency between the two experiments an additional pressure orifice at the bottom side of the airfoil is used.

A wake rake is employed to determine the drag coefficient allowing the comparison with PIV measurements in the wake region. The rake consists of five total pressure probes with an internal diameter of 0.6 ± 0.1 mm and a spacing of 20.0 ± 0.1 mm, and is positioned at one chord length downstream of the model. During the run the wake rake is traversed in the vertical direction with steps of about 1 mm, until the wake is completely scanned at a 1 mm resolution.

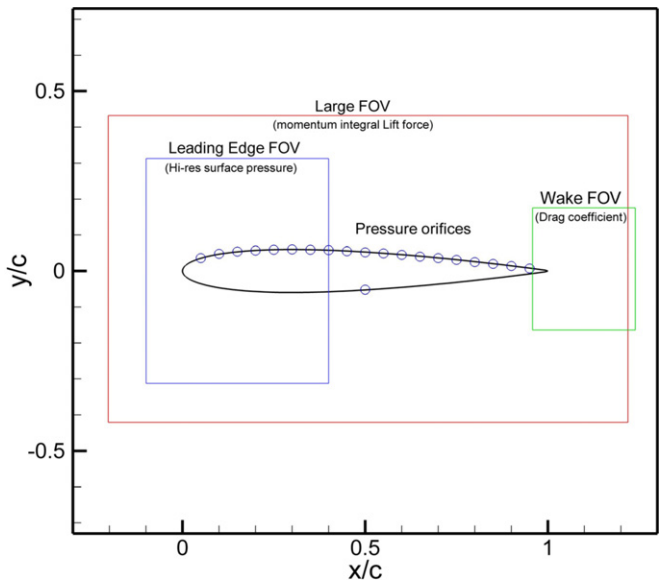

Figure 3. PIV fields of view and position of pressure orifices.

Pressure measurement uncertainty and flow condition variability are the main sources that affect the uncertainty of the reference measurements of the pressure coefficient, defined as

$$C_p = \frac{p - p_\infty}{q_\infty} = \frac{p/p_\infty - 1}{\frac{1}{2}\gamma M_\infty^2} \tag{9}$$

where p_∞ and q_∞ are the free-stream static and dynamic pressure, respectively, and M_∞ is the free-stream Mach number. The pressure in the settling chamber exhibits about 500 Pa of variation (corresponding to 0.25%) during the acquisition time of about 20 s even in the presence of the feedback regulation, whereas the total temperature in the vessel remains constant within 1 K. The pressure

Table 1. Summary of the pressure transducer specifications and pressure uncertainties.

Type	Range (bar)	Digital resolution (bar)	Location	Measured quantity	Uncertainty on the quantity (bar)	Relative uncertainty (%)
PDCR 22	±1	1/8100	Airfoil pressure taps	Static pressure	0.01	0.7
PDCR 22	±1	1/25 000	Wake rake	Wake Pitot pressure	0.01	1.0
PDCR 23	±1.75	1/2660	Nozzle sidewall	Reference static pressure	0.01	0.7
PDCR 80	±10	1/1600	Settling chamber	Total pressure	0.02	2.0

Table 2. PIV parameters and processing settings.

	LFOV	LEFOV	WFOV
Field of view (mm^2)	150 × 150	50 × 50	30 × 30
Optical magnification	0.14	0.41	0.68
Digital magnification (pixel mm^{-1})	6.5	18.5	29.3
Pulse delay (μs)	6	4	3
Free-stream pixel displacement (pixel)	8	15	18
Type of image processing	Pair correlation	Ensemble (2°, 4°) and pair (6°) correlation	Pair correlation
Ensemble size (images)	500	500	500
Final interrogation window (pixel)	31 × 31	2°, 4°: 15 (x) × 5 (y); 6°: 31 × 31	31 × 31
Overlap (%)	75	50	75
Grid spacing (mm)	1.2	2°, 4°: 0.41 × 0.14; 6°: 0.78 × 0.78	0.26

measurements on the orifices are taken sequentially through the run, by means of a scanning valve device. Simultaneously, the pressure in the settling chamber as well as a reference static pressure in the tunnel nozzle wall are recorded, and from their ratio the free-stream Mach number determination is derived based on a previous calibration of the wind tunnel. Table 1 summarizes the specification of the pressure measurements, including instrumentation characteristics; uncertainty estimates in the final properties are primarily those resulting from the operation variability referred to above. The final uncertainty estimate on the individual values of the pressure coefficient is estimated to be below 0.02.

3.2. PIV arrangement

The PIV experimental set-up is schematically depicted in figure 2, showing the model positioned in the wind tunnel test section and the laser light sheet entering from an optical access in the bottom wall downstream of the test section. The three fields of view chosen for the investigation are shown in figure 3 in relation to the airfoil geometry (see further details in table 2). A large field of view (LFOV) captures the velocity field around the entire airfoil, permitting us to place an integration contour around the model in order to compute the integral forces (lift). The leading edge field of view (LEFOV) provides a relatively high spatial resolution in the flow allowing the evaluation of the pressure coefficient on the surface of the airfoil in its leading edge section. The wake field of view (WFOV) is applied to derive the drag coefficient by the wake momentum deficit approach, for which a large magnification with accompanying high spatial resolution is applied. Table 2 summarizes in relation to the different FOV configurations some of the most relevant parameters of the PIV arrangement and the image interrogation procedure.

Tracer particles are distributed by a seeding rake placed in the settling chamber. The PivTec PIVpart 45 seeding generator is equipped with 12 Laskin nozzle delivering droplets of di(2-ethylhexyl) sebacate (DEHS) with about 1 μm mean diameter. The flow is illuminated by a Quantronix Darwin Duo Nd-YLF laser (pulse energy at 1 kHz 25 mJ, wavelength 527 nm, nominal pulse duration 200 ns). Image pairs are acquired at a repetition rate of 500 Hz to form ensembles of uncorrelated data. The light sheet is introduced into the tunnel through a prism located below the lower wall of the wind tunnel. The laser sheet thickness is approximately 2 mm in the test section. The flow is imaged using a Photron FastCAM SA1 CMOS (1024 × 1024 pixels, 12 bit). A Nikon lens with a focal length of 105 mm is used at $f = 2.8$. At this aperture and with a pixel size of 20 μm, particles that are imaged in focus form a diffraction disk of less than a quarter of the pixel size, leading to the undesired phenomenon of peak locking (Westerweel *et al* 1997). To mitigate this effect, the plane of focus is slightly displaced from the measurement plane yielding particle images of approximately 2 pixels diameter. The particle displacement corresponding to the free-stream velocity ranges from 8 pixels (1.2 mm) for the LFOV to about 18 pixels (0.6 mm) for the WFOV.

The image pairs from the LFOV and WFOV are interrogated with an image deformation iterative multigrid technique (WIDIM, Scarano and Riethmuller, 1999) yielding the mean velocity field and turbulent quantities from the ensemble statistics. In the LEFOV, two different procedures have been applied. For an angle of attack of 6°, since the shock exhibits large unsteady fluctuations, again the standard pair-correlation is performed, and the average velocity field is computed. In the other two cases ($\alpha = 2°$ and 4°), steady flow conditions allow us to apply ensemble correlation (Meinhart *et al* 2000) which offers the advantage of a significant improvement in the spatial resolution. In addition, stream-wise elongated windows are used to further increase the resolution in the wall-normal direction.

For an integral momentum approach, it is necessary to measure the velocity field along a closed contour

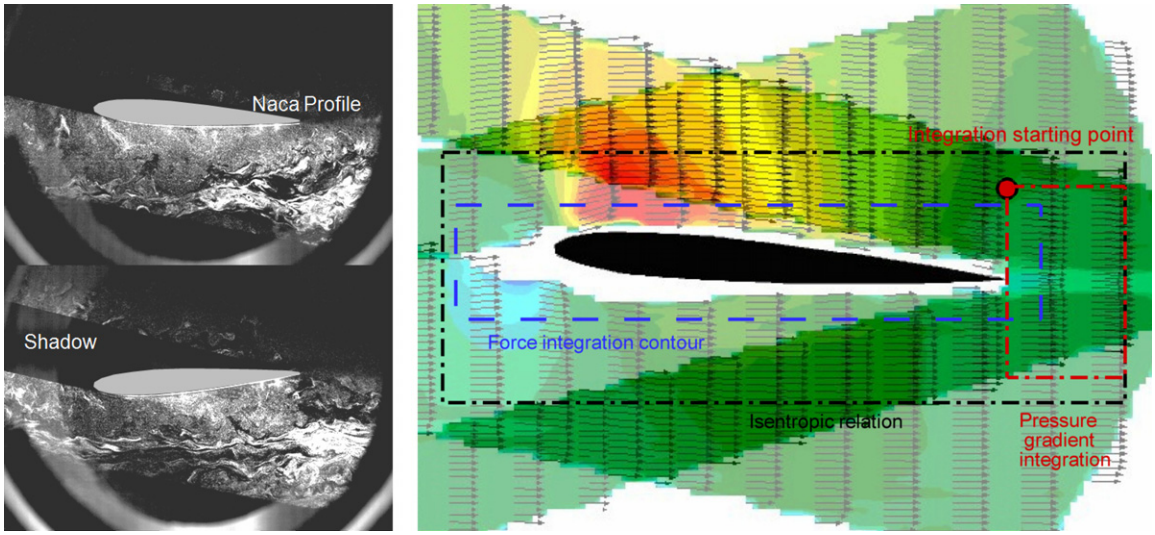

Figure 4. Left: PIV recordings at +4° and −4° angle of attack; right: velocity fields superimposed; black dash-dot: region where isentropic formulation is used; red dash-dot: wake region where pressure gradient integration is applied; blue dash: contour for the integral force evaluation.

encompassing the model. Due to restrictions in optical access, shadow regions are present in the imaged flow field. As a result of this, a part of the flow domain at the shadow side of the airfoil is obscured in the measurement (see figure 2). Therefore, the complete mean velocity field distribution is obtained combining two separate experiments with the airfoil under positive and negative incidence, respectively, taking care that the superimposition of the two images does not introduce any discontinuity at the junctions. In the resulting velocity field, the region which is influenced by reflections or with low signal to noise is blanked and excluded from further data reduction. As an illustration of this procedure, figure 4 shows the velocity fields obtained along the suction and pressure sides of the airfoil in the two separate experiments, as well as the combined result, for an angle of attack of 4°.

3.3. Pressure and load determination procedures

Figure 4 (right) further illustrates the pressure determination and load integration procedures as applied in the LFOV. The large rectangular contour indicates the cutout of the measurement domain of the LFOV that is considered for further evaluation. In most of the inner part of that region, the flow field is treated as isentropic, whereas in the wake region, indicated by the red rectangle, the pressure is determined from integration of the pressure gradient with the marching scheme. The extent of this region is determined by applying a threshold in the values of the vorticity field derived from the PIV measurements, since here the values themselves are not supposed to be negligible. Isentropic boundary conditions for the pressure integration are applied at the top-left corner. The lift force calculation using the contour integral approach is carried out along the closed blue rectangular contour indicated in the figure.

In the LEFOV experiments, the flow field is treated as isentropic and the pressure is computed from the isentropic relation given by equation (7). In the WFOV, on the other hand, the pressure is obtained by the spatial integration of the pressure gradient according to equation (8), with boundary conditions imposed to the bottom and/or top edges of the field of view (see section 5.2 for more details).

4. PIV measurement uncertainty analysis

When pressure fields and integral loads are inferred from the PIV velocity measurements, the uncertainties in these quantities are related to the ones introduced by the velocity measurement itself and by the data reduction procedures, since they propagate in the derived quantities. The following section discusses the nature and impact of the most relevant sources of PIV measurement uncertainty.

4.1. PIV measurement uncertainty

Measurement uncertainties on the PIV velocity data contain random and bias components; the most relevant causes and their estimated effects on the present PIV velocity fields are summarized in table 3. Random components are primarily due to cross-correlation uncertainty and results from flow variability and (turbulent) velocity fluctuations. As a consequence of statistical convergence, the effect of these random uncertainty components decreases with the square root of the number of samples (here $N = 500$). For the cross-correlation uncertainty, a typically value of 0.1 pixel standard error is associated with a three-point fit of the correlation peak (Westerweel 1993). The turbulence effect on the mean value convergence is assessed based on an assumed turbulence level of 10%, which is evidently a conservative choice because of the limited regions in the flow field which displays such a relative high value. The free-stream turbulence level for this tunnel was determined to be below 1%; hence, the overall uncertainty on the mean velocity due to random components is assessed at 0.1% of the free-stream velocity for steady flow

Table 3. Summary of measurement uncertainty contributions for the velocity mean values.

Uncertainties		Error estimator	Typical value	Mean velocity uncertainty (m s^{-1})	Velocity uncertainty relative to V_∞ (%)
Random components	Cross-correlation	$\left[\frac{\varepsilon}{\sqrt{N}}\right]$	$\varepsilon = 0.1$ pixel	0.1	0.05
	Statistical convergence	$\left[\frac{\sigma_u}{\sqrt{N}}\right]$	$\sigma_u = 10\%$	1	0.5
	(turbulent velocity fluctuations)				0
Systematic components	Peak locking	$\left[\frac{d_\tau}{\Delta_{\text{pix}} M \Delta t}\right]$	0.05–0.15 pixel	0.5–4	$\leqslant 2$
	Image matching		0.1 pixel	2	1
	Spatial resolution	$[w_s/\lambda]$	$\lambda \sim 5$ to 10 mm	4–20	2 to 10
	Particle slip	$[\tau\, \vec{V}(\nabla\vec{V})]$	$\tau = 2$ to 3 μs	$\leqslant 20$	$\leqslant 10$
	Aero-optical aberration	$(\vec{V}\cdot\nabla)\vec{\xi}$		$\leqslant 15$	$\leqslant 9$

regions and below 1% of the free-stream velocity in turbulent regions.

The most relevant sources of systematic uncertainties in the PIV measurements are considered to be peak locking, inaccurate image combination, lack of spatial resolution, particle tracers slip and aero-optical aberration. The latter two effects are especially pertinent in the view of the high-speed flow conditions.

Under the present imaging conditions peak locking is to be expected as a significant source of systematic error on the velocity measurement. Defocusing is used to alleviate this effect. The analysis of the resulting velocity histograms allows us to asses that the peak-locking error varies from about 0.05 pixels for the WFOV to about 0.15 for the LFOV; the equivalent velocity error is about 0.5 m s^{-1} and about 3.7 m s^{-1}, respectively. The uncertainty in image superposition, applied to generate the complete velocity fields in the case of the LFOV, is estimated at 1 pixel. Finally, the uncertainty related to spatial resolution is determined by the ratio of the interrogation window size (ws) to the spatial wavelength (λ) of the flow feature under investigation (Schrijer and Scarano 2008). It hence depends strongly on the location in the flow, and for the present investigation is important especially in the wake region as well as near shocks.

These figures provide typical levels of velocity uncertainty as long as the tracer particles follow the flow. In the case of large acceleration $\vec{a}_p$, the flow tracing fidelity is compromised. This particle lag effect results in a systematic velocity error (slip velocity $\vec{V}_{\text{slip}}$), which may be assessed on the basis of the equation of motion for the particle (Melling 1997):

$$\vec{a}_p = \frac{\mathrm{D}\vec{V}_p}{\mathrm{D}t} \approx \frac{\vec{V}_{\text{slip}}}{\tau} = \frac{\vec{V}_f - \vec{V}_p}{\tau} \tag{10}$$

where $\vec{V}_f$ is the velocity of the fluid immediately surrounding the particle traveling at velocity $\vec{V}_p$. The response time τ depends critically on the size and density of the particle, and due to significant uncertainties in these properties, especially for particles formed from agglomerated clusters, one usually determines the response time experimentally by measuring the velocity transient in response to a shock wave (Scarano and van Oudheusden 2003). For the particles used in the present investigation a typical value of the response time is of the order of 3 μs (Schrijer and Scarano 2007). Knowing the value of the time response, the velocity error introduced by slip may now be assessed from the particle acceleration, which can be determined from the measured velocity field under steady flow assumptions:

$$\vec{V}_{\text{slip}} \approx \tau \frac{\mathrm{D}\vec{V}_p}{\mathrm{D}t} = \tau(\vec{V}\cdot\nabla\vec{V}). \tag{11}$$

It was assessed that in the present experiments regions occurred where the particle slip constitutes an appreciable velocity error, not only when a shock is formed, but also in the region of the suction peak around the airfoil at high incidence. For example, at $\alpha = 6^\circ$ values of the slip velocity up to 20 m s^{-1} were inferred locally, which corresponds to 10% of the free-stream velocity.

Moreover, the highest acceleration regions correspond to the highest gradients in density, hence of the refractive index. This introduces additional aero-optical aberration effects which distort the acquired images and affect the velocity field computation by the PIV correlation algorithm (Elsinga *et al* 2005), resulting in a velocity error:

$$\Delta\vec{V}_P(x, y) \approx (\vec{V}_P\cdot\nabla)\vec{\xi} \tag{12}$$

where $\vec{\xi}$ is the optical displacement field caused by the light ray deflection. Relating the refractive index n to the density according to the Gladstone–Dale relation, i.e. $n = 1 + K\rho$ (where $K = 2.3 \times 10^{-4}$ m^3 kg^{-1} for air), and assuming two-dimensional flow, the velocity error can be related to the density gradient field as (Elsinga *et al* 2005)

$$\Delta\vec{V}_P(x, y) \approx -\tfrac{1}{2}KW^2(\vec{V}_P\cdot\nabla)\vec{\nabla}\rho \tag{13}$$

where W is the distance between the measurement plane and the tunnel window, here equal to half the test section width. Using the isentropic flow relations, the density field may be inferred from the velocity field, which in turn allows a first-order estimate of the optical distortion errors to be made. Not surprisingly, the maximum error is found in the shock region; however, the velocity and hence the density gradient fields are extremely unreliable in this region. More reliable values of about 10 m s^{-1} are detected as typical for the suction peak in the leading edge region, for the case of $\alpha = 6^\circ$.

4.2. Pressure and integral loads uncertainty

As in most of the flow domain, the pressure is computed by means of the isentropic relation; the error propagation

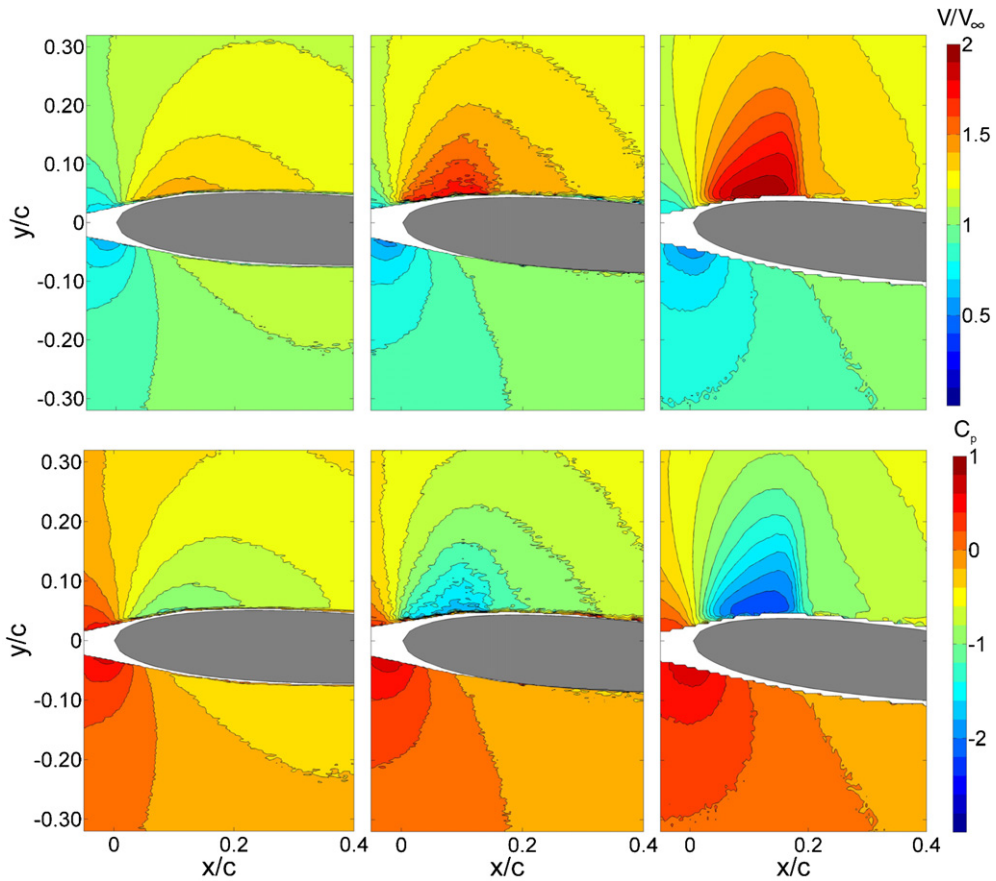

Figure 5. Contours of velocity magnitude (top) and C_p obtained from the isentropic relation (bottom); left to right: $\alpha = 2^\circ$, 4° and 6° (LE zoom configuration, Mach = 0.6).

associated with this method is assessed by a straightforward sensitivity analysis, yielding the following relation between the velocity error and the error in the pressure coefficient:

$$\Delta C_p = -2\frac{p}{p_\infty}\frac{M^2}{M_\infty^2}\cdot\frac{\Delta V}{V}. \tag{14}$$

This shows that a typical order of magnitude of uncertainty error in the pressure coefficient is equal to the relative error of the underlying flow velocity data, which is typically 1% (hence 0.01 in C_p).

Whereas the isentropic relation is clearly not applicable in the viscous flow regions, for which reason it is only applied in the external flow outside the wake, an error may also be introduced in the external flow when it is applied in regions where total pressure losses have been experienced as a result of shock formation. A general expression for the error in C_p resulting from not accounting for losses in total pressure can be formulated, by considering that the isentropic pressure in that case should be corrected by a factor $(1-\varepsilon_{\mathrm{pt}})$, which yields

$$\begin{aligned}\Delta C_p = C_p - C_{p,\mathrm{isen}} &= -\varepsilon_{\mathrm{pt}}\frac{(p/p_\infty)_{\mathrm{isen}}}{\frac{1}{2}\gamma M_\infty^2}\\ &= -\varepsilon_{\mathrm{pt}}\left(\frac{2}{\gamma M_\infty^2} + C_{p,\mathrm{isen}}\right)\end{aligned} \tag{15}$$

where $\varepsilon_{\mathrm{pt}}$ is the relative reduction of the total pressure with respect to its free-stream value:

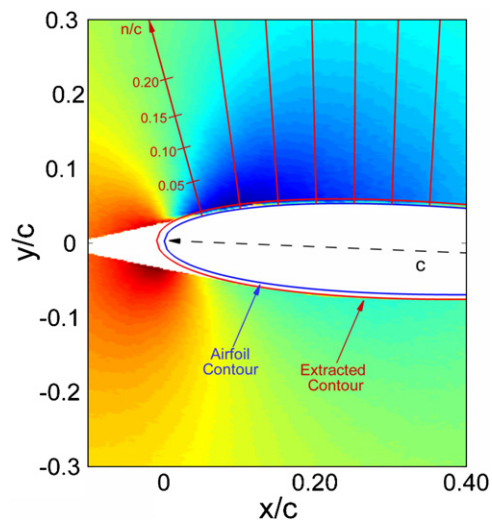

Figure 6. C_p extraction along lines normal to the airfoil contour.

$$\varepsilon_{\mathrm{pt}} = \frac{p_{t,\infty} - p_t}{p_{t,\infty}}. \tag{16}$$

The maximum uncertainty on the C_p fields varies with location, from about 0.003 to 0.015 in $\alpha = 2^\circ$ and from about 0.025 to 0.2 in $\alpha = 6^\circ$. Finally, the uncertainty in the aerodynamic loads was assessed by applying a linear error propagation analysis

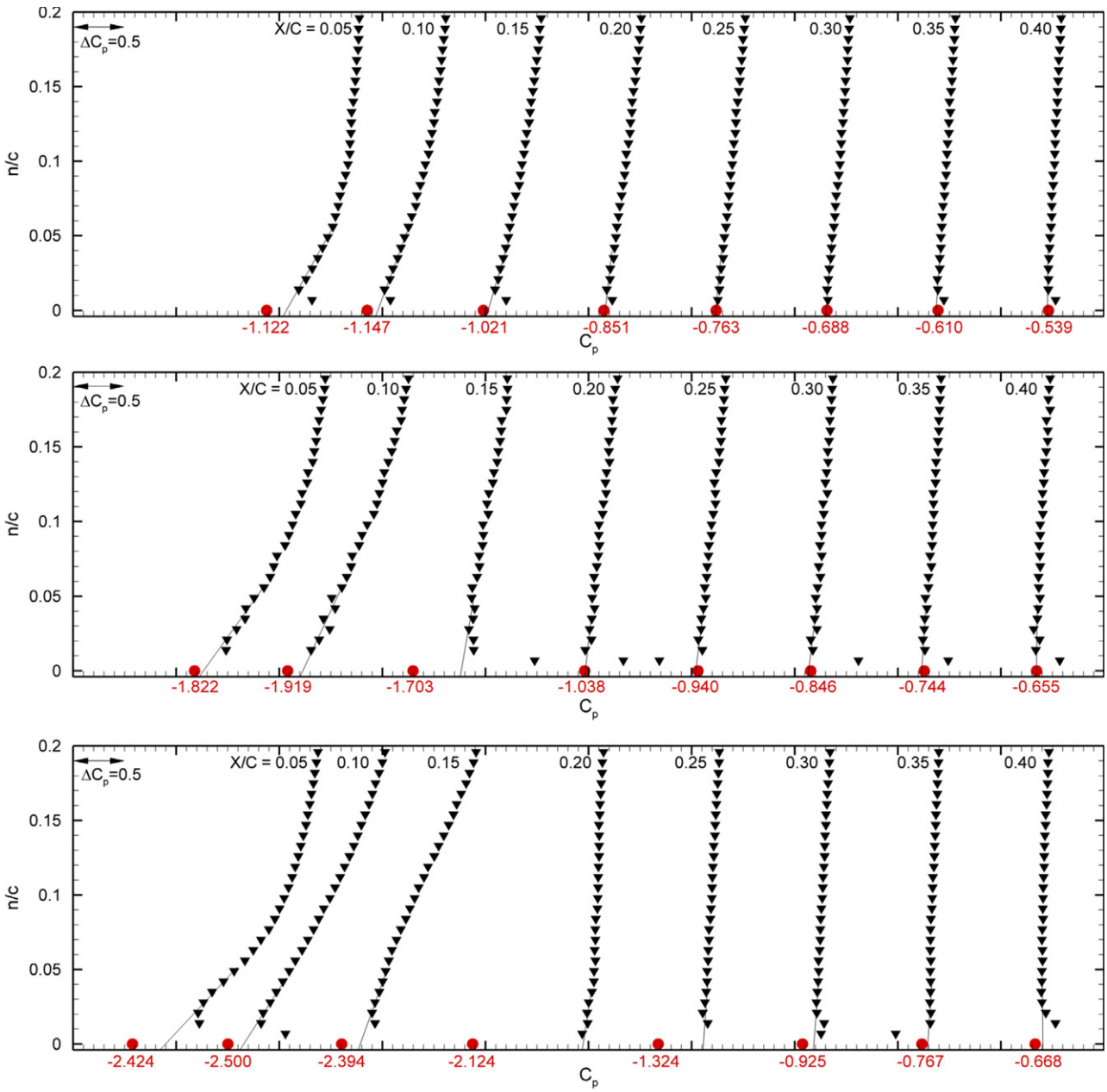

Figure 7. Pressure compared through lines normal to the profile; red dots: surface pressure transducers; black triangles: PIV-based pressure based on the isentropic relation.

based on the estimated errors in velocity and/or pressure, as determined above. The results of this analysis, shown as error bars in figure 10, indicate a typical uncertainty of about 0.04 on C_l, and of about 0.004 on C_d.

5. Results

This section presents the results of the PIV experiments for $M = 0.60$. The first section deals in particular with the comparison of the surface pressure from the PIV velocity measurements, based on the LEFOV geometry with the reference measurement provided by the pressure orifices. The second section is devoted to the computation of integral forces (lift and drag) from contour and wake defect approaches.

5.1. Surface pressure determination

In order to compare directly the surface pressure measurement with the ones computed from PIV a relatively high spatial resolution in the leading edge region has been used (LEFOV configuration). The digital imaging resolution involved is about 11.9 pixels mm^{-1}, implying about four vectors per mm with 50% window overlap. The PIV fields in figure 5 show the time-averaged velocity fields (top) and the corresponding patterns of the pressure coefficient (bottom), when increasing the angle of attack from 2° to 6° (left to right). The pressure has been determined in this case from direct application of the isentropic relation. At high Reynolds number the boundary layer thickness is very small (under the present flow

conditions on the order of 0.1 mm at 10% of the chord), so the isentropic assumption should be correct up to very close to the surface, provided no separation takes place and in the absence of shocks. The depicted results reflect the typical flow structure around an airfoil in the transonic regime and its evolution with increasing angle of attack. The measurements at an angle of attack of 2° show a pressure map with the maximum value of C_p near the critical condition ($C_{p,\mathrm{crit}} = -1.29$ at $M = 0.6$); therefore, a pocket of supersonic flow is expected to develop for higher angles of attack. Increasing the angle from 2° to 6° further, compressibility effects become evident; notably the shape of the expansion region on the suction side is deformed, exhibiting a supersonic pocket terminating by a quasi-normal shock wave. At $\alpha = 6°$, the inspection of the instantaneous velocity snapshots reveals that the shock oscillates considerably, which requires to revert to the pairs correlation averaged results, in contrast to the ensemble correlation technique used at $\alpha = 2°, 4°$. The shock unsteadiness is also reflected in the apparent broadening of the shock region in the time-averaged velocity and pressure fields.

To assess the potential of PIV in determining the pressure close to the surface, the pressure fields of figure 5 have been further analyzed by extracting the pressure distribution along lines normal to the airfoil contour. The lines along which the pressure is extracted correspond to the available pressure orifice positions and are shown in figure 6, superimposed over the pressure contour plot. The extracted pressure profiles are plotted in figure 7 (black triangles), where the pressure orifice measurements are given by red circles. The corresponding surface pressure distributions are plotted in figure 8.

As stated previously, the isentropic conditions may apply up till close to the surface, and the PIV based pressure data in figure 7 are found in good agreement with the surface pressure transducers except from some anomalies at $\alpha = 6°$, which will be discussed later. However, PIV measurements close to the surface become unreliable due to reflections and edge effects and this is reflected in the increased scatter of the pressure data close to the wall. Therefore PIV-based surface pressure distributions are provided in figure 8 where data were taken at a relatively larger distance from the surface (∼1 mm = 1% chord). This distance introduces a significant deviation from the actual surface pressure when the pressure gradient normal to the surface is large, which is especially the case in the leading edge region. When using a linear extrapolation of the PIV data down to the surface, a better match with the measurements from the pressure orifices is obtained. In conclusion, the results in figures 7 and 8 show that this extrapolation procedure corrects the PIV-based pressure distribution significantly, and brings it to values comparable to the pressure orifices within a few percent. This level of agreement is obtained for the entire airfoil for the 2° and 4° angle of attack cases, as well as for the 6° angle of attack case at the lower surface and upstream of the shock region.

For the 6° angle of attack case the PIV measurements reveal the presence of a well-defined shock wave on the upper surface at approximately $x/c = 0.20$ (see figure 5 top right). Under these circumstances, as a result of the total pressure loss over the shock, the isentropic assumption is expected to introduce errors on the C_p determination on the surface, while simultaneously a significant deviation between PIV based and transducer surface pressure measurement is observed, notably for the position $x/c = 0.20$ and $x/c = 0.25$ (see figure 7). Before assessing the potential impact of the

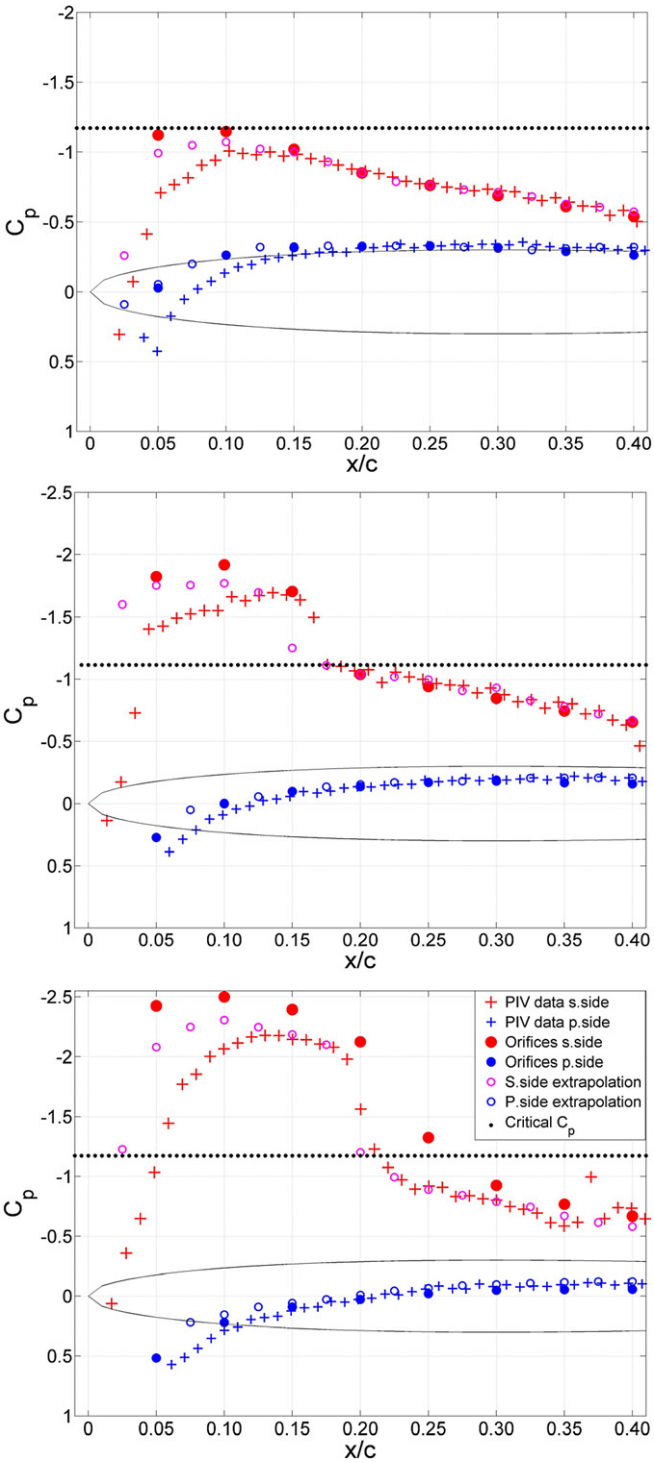

Figure 8. Pressure distribution comparison (blue symbols: pressure side; red symbols: suction side); filled dots: pressure orifice data; crosses: PIV-based data taken at 1 mm from the surface; open circles: PIV-based data extrapolated toward the surface; black dotted line: critical C_p.

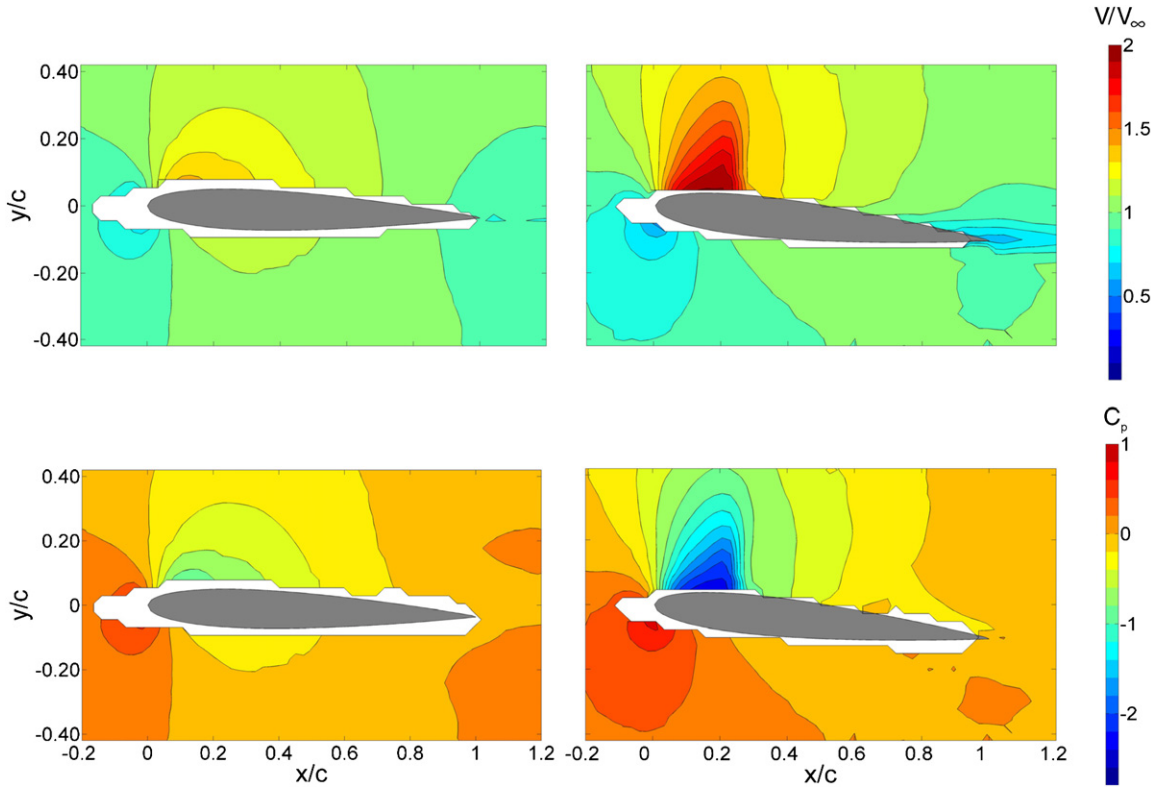

Figure 9. Large field of view, $M = 0.6$; $\alpha = 2^\circ$ on the left, 6° on the right.

shock-induced total pressure losses not accounted for by using the isentropic pressure relation, it is necessary to realize the reported unsteadiness in shock position. It is not unlikely that this does not have the same impact on the averaged velocity field obtained with the PIV method as it does on the pressure measurement system, due to different systems characteristics. Also, the isentropic relation does not take the effect of velocity fluctuations induced by the oscillating shock into account. In order to estimate the error introduced by using the isentropic relation for the PIV based pressure computation, the shock Mach number is inferred to be about $M = 1.3$, based on the upstream flow conditions. According to shock theory the velocity accordingly changes from 1.94 V_∞ upstream of the shock to 1.28 V_∞ downstream of it, which agrees well with the PIV measurements (see figure 5 top right). The associated change in the pressure coefficient is from $C_p = -2.14$ upstream to $C_p = -0.67$ downstream. Using the isentropic relation a downstream value of $C_p = -0.60$ would have been obtained. This difference between the expected and isentropic pressure coefficient values agrees with the error estimation from section 4.2, where for this shock strength the total pressure loss over the shock is only 2%. It is hence evident that it is not so much the total pressure loss over the shock that is responsible for the observed differences between PIV-based pressure and the pressure orifice results. Rather, the unsteady character of the shock wave introduces seriously uncertainties on both techniques, for which reason we should discard this region for the present validation. Note that good agreement between the two methods is again obtained from $x/c = 0.30$ onward.

5.2. *Integral force determination*

In order to compute the integral lift force by means of the contour approach, a field of view encompassing the airfoil is needed, which is provided by the LFOV imaging condition. In figure 9, velocity and pressure coefficient contours of the large field of view are presented. The velocity fields show a similar flow structure around the airfoil as in the LEFOV configuration, but with an evidently lower spatial resolution. However, when the data away from the airfoil are considered, the constraint on spatial resolution can be relaxed to a large extent, except for the wake region, where the LFOV resolution is insufficient to describe the velocity defect even at the most downstream location available. This would strongly affect the drag computation from the contour approach, but has no appreciable impact on the lift computation.

The lift coefficient obtained from the PIV-based contour approach is compared with the lift derived from the surface pressure distribution provided by the pressure taps in figure 10 (left). At $\alpha \leqslant 3^\circ$, the lift coefficient computed by the PIV-based method agrees with those derived from pressure orifices within a few percent. For the higher angles of attack it is possible to observe an increased difference, with the PIV method systematically yielding higher values of the lift with respect to the reference measurement.

In addition, reference data from an AGARD database have been considered as a verification of the present airfoil characteristics measurements. These experiments were performed at comparable Mach and Reynolds numbers on a NACA 0012 airfoil at the ONERA S3 facility. For a valid

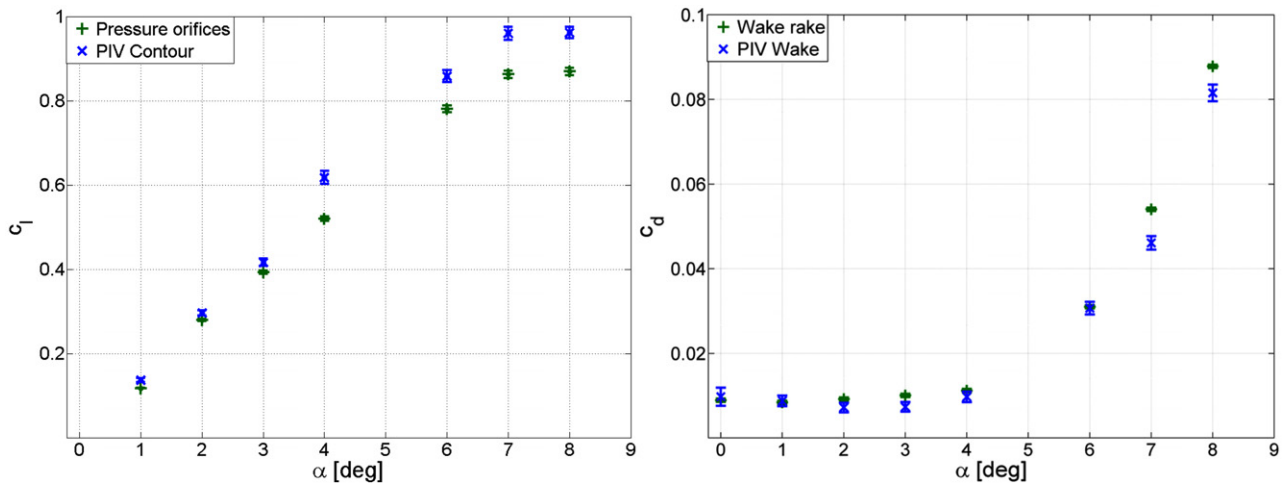

Figure 10. Lift (left) and drag (right) coefficient comparison versus α—PIV versus pressure orifices.

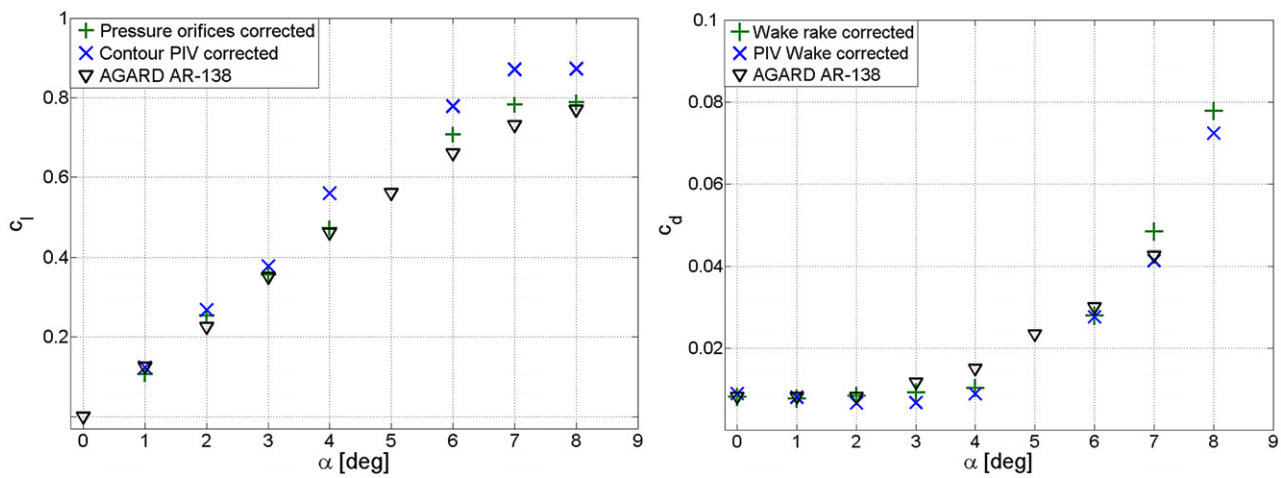

Figure 11. Lift (left) and drag (right) coefficient versus α—corrected for the blockage effect.

comparison, the present data need to be corrected for blockage though. The blockage ratio is 5% for the present experiment whereas it was only 0.3% at S3. Once corrected, using a simple model and a wake blockage correction procedure, the measurement mismatch is reduced and pressure orifices data agree within a few percent with the reference ones, while PIV data are still showing a slight over-prediction.

The diagrams in figures 10 and 11 (right) contain the drag coefficients obtained with the wake approach, validated against the Pitot pressure rake method. Given the low scaling factor and the window size adopted, the contour approach for the drag coefficient determination suffers from a severe lack of resolution, giving motivation to use the wake field of view in the PIV computation, as discussed in section 2.1. Unlike the large field of view the wake zoom is able to capture the defect in the velocity in a more resolved way. Figure 12 presents the velocity and pressure fields from the wake zoom from which the steep velocity gradient in the near wake and the recovery toward the edge of the field of view are noticeable. The higher spatial resolution is fundamental for the data reduction procedure, in which a zonal approach is used, dividing the field of view into isentropic (irrotational) and non-isentropic (rotational) regions. In cases where the extent of the wake is not clearly defined or not captured by the field of view, the uncertainties in the drag coefficient computation become much larger.

In order to decrease the accumulation of error in the marching procedure of the pressure-integration scheme, isentropic flow conditions are assumed at a certain distance above and below the trailing edge of the airfoil for angles of attack up to about 4°. Then equation (8) is used to integrate the pressure gradient field in order to obtain the pressure in the wake region. The two integration fronts, starting from the opposite sides of the wake, meet at the wake center line, introducing a small pressure mismatch there. At larger angles of attack the entire upper region of the field of view can no longer be treated as isentropic, being affected by viscous effects, shock formation or flow separation. In that case the isentropic flow condition is only imposed below the wake and an upward integration is carried out. This unidirectional integration approach increases the error propagation, hence the uncertainty in the pressure in the wake region.

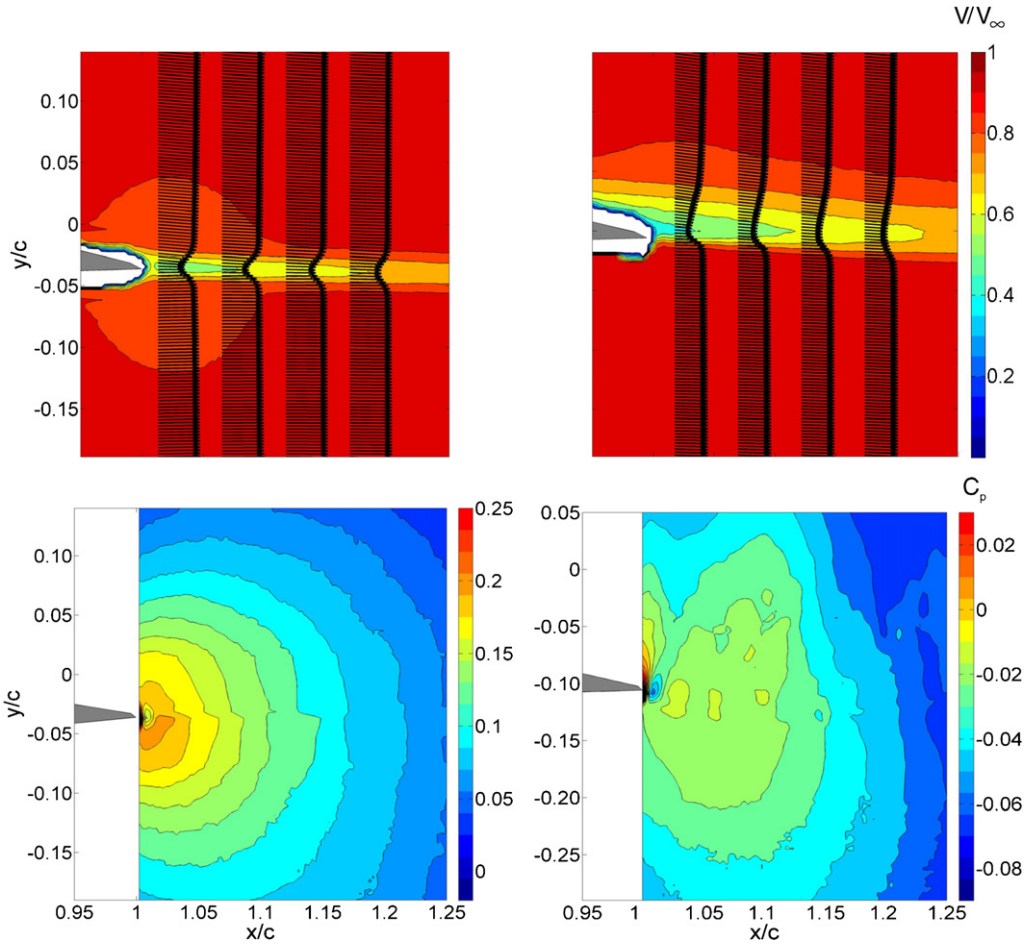

Figure 12. WFOV velocity (top) and C_p (bottom) distribution: (left) $\alpha = 2^\circ$, (right) $\alpha = 6^\circ$.

The drag coefficient computed using the PIV wake zoom, presented in figure 10, shows good agreement with the Pitot-probe wake rake at smaller angles and also with the literature when corrected for blockage (figure 11). Even at the larger angles of attack there is good agreement between the wake rake and PIV in the wake. Further analysis has been carried out to assess the sensitivity of the drag coefficient computation on the distance from the trailing edge where the integral is evaluated. For distances more than 10% of the chord from the trailing edge the values of the drag coefficient does not change appreciably with the choice of the downstream position, which consolidates the proposed procedure.

Investigating the different contributions to the lift and drag computation, it was found that for the lift the main contributions come from both the pressure and mean momentum terms on the top and bottom 'legs' of the rectangular integration contour. It is interesting to note that, in contrast to the momentum deficit concept suggested by equation (4), actually the determination of the static pressure has an important impact on the drag computation as well. Finally, it was found that including the turbulent stresses in the computation of the forces did not affect the results within experimental uncertainty as long as no appreciable flow separation occurs.

6. Conclusions

PIV experiments have been conducted on an airfoil model in the transonic flow regime with the objective to use velocimetry data to infer the surface pressure distribution as well as aerodynamic loads. This requires pressure evaluation, which can be carried out with the isentropic relation in the case of attached inviscid flow, and with integration of the Euler equations in rotational flow regions, notably the airfoil wake. Integral aerodynamic loads can be obtained from contour integrals, for both lift and drag, but the drag is more accurately and more conveniently derived from a wake defect approach. Three different fields of view have been used at different spatial resolution to determine 2D velocity vector fields from which to compute the surface pressure coefficient, the lift and drag coefficient. The surface pressure shows excellent agreement with the pressure orifices in the absence of shocks, although to correctly capture the pressure on the nose region of the airfoil an extrapolation of the PIV data toward the actual surface is needed, in view of the large pressure gradient normal to the surface and limited spatial resolution. In the presence of shocks, the use of the isentropic relation introduces an error on the pressure values, which remains moderate for mild shock strengths (see e.g. the 6° angle of attack case). For cases with stronger shocks, using the pressure-integration

approach may improve the pressure computation in external flow regions affected by total pressure losses. Lift and drag coefficients can be reliably obtained from PIV, though there is some disagreement between the PIV-based results and the reference measurements. They are currently both estimated to have a 10% error with respect to the conventional loads determination approaches. For the drag coefficient the wake-based formulation is crucial for obtaining accurate results. The pressure term is a dominant factor for both force components, even for the drag determination since the wake measurement plane is relatively close to the airfoil, within one chord length of the trailing edge. Compressible flow effects, notably particle lag and optical aberration, were assessed to have an appreciable potential impact on the PIV velocity measurement. These effects are especially felt near the airfoil surface, where flow acceleration and density gradients are strongest, but as they become progressively less pronounced further away from the airfoil their impact on the force coefficient is not necessarily large.

References

AGARD Advisory report 138. Experimental data base for computer program assessment

Anderson J D 1991 *Fundamentals of Aerodynamics* 2nd edn (New York: McGraw-Hill)

Anderson J D 2003 *Modern Compressible Flow with Historical Perspective* 3rd edn (New York: McGraw-Hill)

Baur T and Köngeter J 1999 PIV with high temporal resolution for the determination of local pressure reductions from coherent turbulent phenomena *3rd Int. Workshop on PIV (Santa Barbara)* pp 671-6

De Gregorio F 2006 Aerodynamic performance degradation induced by ice accretion PIV technique assessment in icing wind tunnel *13th Int. Symp. Appl. Laser Techn. to Fluid Mech. (Lisbon, Portugal)*

Elsinga G E, van Oudheusden B W and Scarano F 2005 Evaluation of aero-optical distortion effects in PIV *Exp. Fluids* **39** 245–56

Jones B M 1936 Measurement of profile drag by the Pitot-traverse method *ARC R&M 1688*

Klein C, Engler R H, Henne U and Sachs W E 2005 Application of pressure-sensitive paint for determination of the pressure field and calculation of the forces and moments of models in a wind tunnel *Exp. Fluids* **39** 475–83

McLachlan B G and Bell J H 1995 Pressure-sensitive paint in aerodynamic testing *Exp. Therm. Fluid Sci.* **10** 470–85

Meinhart C D, Werely S T and Santiago J G 2000 A PIV algorithm for estimating time-averaged velocity fields *J. Fluids Eng.* **122** 285–9

Melling A 1997 Tracer particles and seeding for particle image velocimetry *Meas. Sci. Technol.* **8** 1406–26

Scarano F and Riethmuller M L 1999 Iterative multigrid approach in PIV image processing with discrete window offset *Exp. Fluids* **26** 513–23

Scarano F and van Oudheusden B W 2003 Planar velocity measurements of a two-dimensional compressible wake *Exp. Fluids* **34** 430–41

Schrijer F F J and Scarano F 2007 Particle slip compensation in steady compressible flows *7th Int. Symp. on Particle Image Velocimetry (Rome, Italy)*

Schrijer F F J and Scarano F 2008 Effect of predictor–corrector filtering on the stability and spatial resolution of iterative PIV interrogation *Exp. Fluids* **45** 927–41

Sjörs K and Samuelsson I 2005 Determination of the total pressure in the wake of an airfoil from PIV data *PIVNET II Int. Workshop on the Application of PIV in Compressible Flows (Delft, The Netherlands)*

Souverein L J, van Oudheusden B W and Scarano F 2007 Particle image velocimetry based loads determination in supersonic flows *45th AIAA Aerosp. Science Meeting & Exhibit (Reno, NV)* Paper AIAA-2007-0050

Unal M F, Lin J C and Rockwell D 1998 Force prediction by PIV imaging: a momentum-based approach *J. Fluids Struct.* **11** 965–71

van Oudheusden B W 2008 Principles and application of velocimetry-based planar pressure imaging in compressible flows with shocks *Exp. Fluids* **45** 657–74

van Oudheusden B W, Scarano F and Casimiri E W F 2006 Non-intrusive load characterization of an airfoil using PIV *Exp. Fluids* **40** 988–92

van Oudheusden B W, Scarano F, Roosenboom E W M, Casimiri E W F and Souverein L J 2007 Evaluation of integral forces and pressure fields from planar velocimetry data for incompressible and compressible flows *Exp. Fluids* **43** 153–62

Westerweel J 1993 *Digital Particle Image Velocimetry* (Delft: Delft University Press)

Westerweel J, Dabiri D and Gharib M 1997 The effect of a discrete window offset on the accuracy of cross-correlation analysis of digital PIV recordings *Exp. Fluids* **23** 20–8